hv photonics

IMPACT FACTOR 2.4

CITESCORE 2.3

Communication

Generation of Second-Order Sideband through Nonlinear Magnetostrictive Interaction

Lei Yang, Bao Wang and Hao Xiong

Special Issue
Hybrid Quantum Magnonics

Edited by
Prof. Dr. Jie Li, Prof. Dr. Huatang Tan and Prof. Dr. Hao Xiong

MDPI

https://doi.org/10.3390/photonics10080886

photonics

MDPI

Communication

Generation of Second-Order Sideband through Nonlinear Magnetostrictive Interaction

Lei Yang [1], Bao Wang [1,*] and Hao Xiong [2]

[1] School of Information Engineering, Nanyang Institute of Technology, Nanyang 473004, China
[2] School of Physics, Huazhong University of Science and Technology, Wuhan 430074, China
* Correspondence: baowang@hust.edu.cn

Abstract: Nonlinear interaction between the magnon mode and the mechanical mode in a magnomechanical system is treated analytically where the magnon mode is coherently driven by a bichromatic microwave drive field consisting of a strong pumping field and a weak probe field and that works within a perturbative regime. Using experimentally achievable parameters, we show that the magnonic second-order sideband is generated and can be considerably enhanced by increasing the power of the pumping field. The suppression of the magnonic second-order sideband generation at the resonance point is discussed. Furthermore, the efficiency of magnonic second-order sideband generation can be well controlled by adjusting the applied bias magnetic field strength, which is a particular feature compared to the optical second-order sideband. In addition to offering insights into the magnomechanical nonlinearity, the present results have the potential to pave the way for exploring practical applications for achieving high-precision measurement in magnonics.

Keywords: magnetostrictive effect; perturbation method; second-order sideband

Citation: Yang, L.; Wang, B.; Xiong, H. Generation of Second-Order Sideband through Nonlinear Magnetostrictive Interaction. *Photonics* **2023**, *10*, 886. https://doi.org/10.3390/photonics10080886

Received: 13 July 2023
Revised: 27 July 2023
Accepted: 30 July 2023
Published: 1 August 2023

1. Introduction

A spin wave is the collective excitation of magnetization in ordered magnets, and a magnon is the spin wave quanta [1–3]. The ferrimagnetic insulator yttrium iron garnet (YIG) with high spin density, very low magnetic damping, and a high Curie temperature provides an alternative platform for quantum information processing [4–7]. The utilizaton of a magnon as a carrier to transmit and process information is an emerging research field in spintronics [1]. Coherent coupling between magnons and microwave photons through magnetic dipole interaction has been demonstrated experimentally in a three-dimensional microwave cavity coupled with a YIG sphere [6], where the interplay can achieve a strong and even an ultrastrong coupling regime, leading to cavity-magnon polaritons [7]. Many important physical phenomena, such as Rabi oscillation, magnetically induced transparency, the Purcell effect [4], and magnon gradient memory [8], have been reported in cavity magnonics based on coherent coupling. Moreover, due to the powerful compatibility of magnons, optical photons [9–15] and superconducting qubits [16–18] can be coherently coupled to magnons, which offers the prospect of fabricating new hybrid quantum systems.

The magnetostrictive effect describes the phenomenon that, when the magnon mode in the YIG sphere is excited, the varying magnetization induced by the magnon excitation leads to geometrical deformation of the YIG sphere, which can be treated as a mechanical resonator [19]. Currently, the magnomechanical system [20–24], which describes the coherent coupling between magnon modes and mechanical modes (phonons) in the YIG sphere via the magnetostrictive effect, has attracted extensive attention in the magnonic field and many exciting advances have been achieved, These include achieving magnon–photon–phonon entanglement [25–27], mechanical bistability [28], nonreciprocal transmission [29–32], squeezing of the microwave field [33], and magnonic frequency

combs [34–36]. On the other hand, non-Hermitian cavity magnonics has also aroused considerable interest and has emerged as a new frontier in the magnonic field [37–40]. Non-Hermitian cavity magnomechanical systems have been proposed to generate magnon chaos [41], enhance sideband responses [42], and manipulate optical transmission [43]. It is well known that nonlinear phenomena can offer insights into understanding of the magnon–phonon interaction and can help promote the development of cavity magnomechanics.

In the present work, we theoretically investigate an important nonlinear effect, the second-order sideband in a magnomechanical system. We obtain the analytical expression for the amplitude of the magnonic second-order sideband by employing a perturbation technique. We show that the efficiency of the second-order sideband generation exhibits a strong dependence on the microwave driving field. Moreover, we show that the second-order sideband control can be achieved by adjusting the external magnetic field. All the relevant parameters are well within current experimental reach. Our work establishes a theoretical framework for generating a magnonic second-order sideband and provides a way to study other nonlinear phenomena induced by the magnetostrictive effect and to explore corresponding applications.

2. Physical Setup and Dynamical Equation

We consider a magnomechanical system, as shown in Figure 1a, where a YIG sphere is placed near a port, which is designed for inputting a microwave field to drive the YIG sphere via a superconducting microwave line with a loop antenna. The YIG sphere is magnetized by a uniform bias static magnetic field (along the z direction, i.e., $\boldsymbol{H} = H\hat{z}$) to induce the magnon mode. Due to the finite geometry, the magnetized YIG sphere confines the magnon modes and acts as a magnonic resonator. As a fundamental magnon mode, the Kittel mode is a uniform magnetization precession. The frequency of the Kittel mode is determined by the external bias magnetic field $\boldsymbol{H}$, viz. $\omega_m = \gamma H$, where $\gamma/2\pi = 28\,\mathrm{GHz/T}$ is the gyromagnetic ratio and H denotes the magnetic field strength [6]. For the bias magnetic field ranging from 0 from 1 T, the resonance frequency of the Kittel magnon mode corresponds to 0 to 28 GHz. The quantum mechanical Hamiltonian of the Kittel mode can be expressed as $\hat{H}_m = \hbar\omega_m \hat{m}^\dagger \hat{m}$ via the Holstein–Primakoff transformation [44], where $\hat{m} = \frac{V_m}{2\hbar\gamma M_s}(M_x - iM_y)$ is the annihilation operator of the Kittel mode, with V_m the YIG sphere volume, M_s is the saturation magnetization, and $M_{x,y}$ are the magnetization components. Here, we assume that the Kittel magnon mode of the YIG sphere is excited by a bichromatic microwave drive field, and setting of the magnetic component of the microwave drive field in the $x-y$ plane. The Hamiltonian of the driving of the Kittel mode by the microwave drive fields consisting of the pumping and probe fields is of the form $\hat{H}_d = i\hbar\Omega_0(\hat{m}^\dagger e^{-i\omega_0 t} - \hat{m}e^{i\omega_0 t}) + i\hbar\Omega_p(\hat{m}^\dagger e^{-i\omega_p t} - \hat{m}e^{i\omega_p t})$ within the condition of the low-lying excitations [25], where $\Omega_i = \frac{\sqrt{5}}{4}\gamma\sqrt{N}B_i\ (i = 0, p)$ are the Rabi frequencies denoting the coupling strength between the drive magnetic fields and the magnon mode, where $N = \rho V_m$ is the total number of spins in the YIG sphere, with $\rho = 4.22 \times 10^{27}\ \mathrm{m}^{-3}$ the spin density of the YIG sphere, and B_0 and B_p are the amplitudes of the drive magnetic fields, with frequencies ω_0 and ω_p corresponding to the pumping field and the probe field, respectively. The power of the microwave drive field $P_i = \frac{B_i^2}{2\mu_0}Sc\ (i = 0, p)$, where μ_0 is the vacuum magnetic permeability, c is the speed of an electromagnetic wave propagating through the vacuum, and $S = \pi R^2$ is the cross-sectional area, with R the radius of the YIG sphere; therefore, $B_i = \frac{1}{R}\sqrt{\frac{2P_i\mu_0}{\pi c}}$.

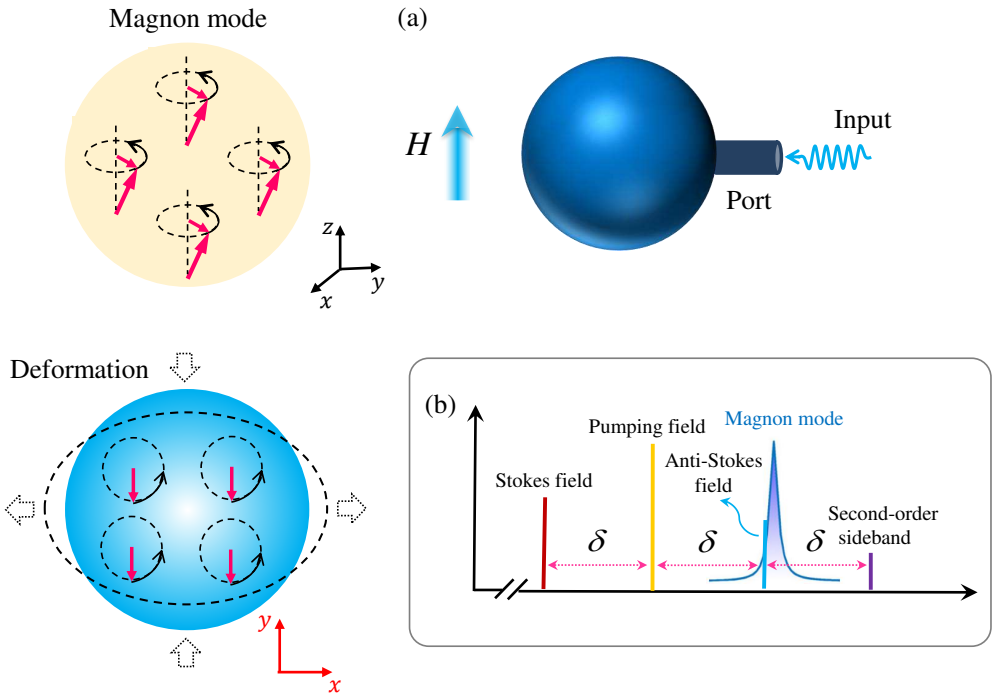

Figure 1. (Color online) (**a**) Schematic diagram of a magnomechanical system. A uniform bias static magnetic field (H) is applied along the z-direction to magnetize the YIG sphere. The magnon mode is directly driven via a microwave antenna. The varying magnetization causes the deformation of the YIG sphere. (**b**) Frequency spectrum of the output fields. The yellow line indicates the frequency of the pumping field ω_0, the red line is the frequency of the Stokes field $\omega_0 - \delta$, and the blue line is the frequency of the anti-Stokes field (the probe field) $\omega_0 + \delta$. The frequency of the probe field is ω_p, and the detuning between the pumping field and the probe field is $\delta = \omega_p - \omega_0$. The violet line is the second-order sideband $\omega_0 + 2\delta$. The frequency of the magnon mode is ω_m.

According to the magnetostrictive effect, the varying magnetization induced by the microwave magnetic field causes deformation of the YIG sphere and the deformation can also change the magnetization, which leads to a nonlinear interaction between the Kittel magnon mode and the vibrational mode. The Hamiltonian of the magnetostrictive interaction can be written as $\hat{H}_{int} = \hbar g_{mb} \hat{m}^\dagger \hat{m} (\hat{b} + \hat{b}^\dagger)$ [20], where $\hat{b}$ is the annihilation operator of the phonon (the quantum of the mechanical vibration mode) and g_{mb} is the single magnon–phonon coupling strength, which is simmlar to the optomechanical interaction [45,46]. In sum, the Hamiltonian of the system includes three parts, i.e., $\hat{H} = \hat{H}_m + \hat{H}_d + \hat{H}_{int}$, which is the starting point of the following discussion.

Based on the above Hamiltonian and by introducing the dissipation with the Markov approximation [47] in a frame rotating with frequency ω_0, i.e., a unitary transformation $\hat{U}(t) = \exp(-i\omega_0 \hat{m}^\dagger \hat{m} t)$ is applied, the Heisenberg–Langevin equations ($\dot{\hat{o}} = \frac{i}{\hbar}[\hat{H}, \hat{o}]$) [48] describing the system dynamics are given by:

$$\frac{d\hat{m}}{dt} = (-i\Delta_m - \kappa_m)\hat{m} - ig_{mb}\hat{m}(\hat{b} + \hat{b}^\dagger) + \Omega_0 + \Omega_p e^{-i\delta t} + \sqrt{2\kappa_m}\hat{m}_{in}, \tag{1a}$$

$$\frac{d\hat{b}}{dt} = (-i\omega_b - \kappa_b)\hat{b} - ig_{mb}\hat{m}^\dagger \hat{m} + \sqrt{2\kappa_b}\hat{b}_{in}, \tag{1b}$$

where $\Delta_m = \omega_m - \omega_0$ is the detuning between the pumping field and the magnon mode, $\delta = \omega_p - \omega_0$ is the detuning between the pumping field and the probe field, ω_b is the frequency of the mechanical mode, and κ_m and κ_b are, respectively, the decay rate of the magnon and the mechanical mode; m_{in} and b_{in} are the noise operators for the magnon and mechanical modes, respectively, which are zero mean, i.e., $\langle \hat{m}_{in}(t) \rangle = 0$ and $\langle \hat{b}_{in}(t) \rangle = 0$, and are character-

ized by the correlation functions $\langle \hat{m}_{in}(t)\hat{m}_{in}^{\dagger}(t')\rangle = [N_m(\omega_m)+1]\delta(t-t')$, $\langle \hat{m}_{in}^{\dagger}(t)\hat{m}_{in}(t')\rangle = N_m(\omega_m)\delta(t-t')$, and $\langle \hat{b}_{in}(t)\hat{b}_{in}^{\dagger}(t')\rangle = [N_b(\omega_b)+1]\delta(t-t')$, $\langle \hat{b}_{in}^{\dagger}(t)\hat{b}_{in}(t')\rangle = N_b(\omega_b)\delta(t-t')$ [47], where $N_{m(b)}(\omega_{m(b)}) = \left[\exp(\hbar\omega_{m(b)}/k_BT)-1\right]^{-1}$ are the equilibrium mean thermal magnon (phonon) number, with k_B the Boltzmann constant and T the environmental temperature. Within the semiclassical approximation, the magnon and phonon operators are reduced to their expectation values [34,49], viz., $m = \langle \hat{m}\rangle$, $m^* = \langle \hat{m}^{\dagger}\rangle$, $b = \langle \hat{b}\rangle$, and $b^* = \langle \hat{b}^{\dagger}\rangle$, and the quantum noise terms can be safely dropped. In addition, the mean-field approximation by factorizing averages, i.e., $\langle \hat{m}^{\dagger}\hat{m}\rangle = m^*m$, is used to deal with the nonlinear term $ig_{mb}\hat{m}^{\dagger}\hat{m}$. Then, the Heisenberg–Langevin equations read

$$\frac{dm}{dt} = (-i\Delta_m - \kappa_m)m - ig_{mb}m(b+b^*) + \Omega_0 + \Omega_p e^{-i\delta t}, \tag{2a}$$

$$\frac{db}{dt} = (-i\omega_b - \kappa_b)b - ig_{mb}m^*m. \tag{2b}$$

Assuming that the pumping field is much stronger than the probe field, we can employ the perturbation method for solving the evolution Equations (2a) and (2b); that is, the solution of the Equations (2a) and (2b) can be written as the sum of the steady-state values and the small perturbations. Physically, the strong pumping field provides the steady-state solutions (m_0, b_0) of the system, and the weak probe field provides the perturbations around the stable states. Accordingly, the total solutions of Equations (2a) and (2b) can be described by $m = m_0 + \delta m$ and $b = b_0 + \delta b$. Setting $dm_0/dt = 0$ and $db_0/dt = 0$, the steady-state solutions of Equations (2a) and (2b) can be obtained as

$$m_0 = \frac{-\Omega_0}{i\Delta_m + \kappa_m - ig_{mb}(b_0 + b_0^*)}, \tag{3a}$$

$$b_0 = \frac{-ig_{mb}|m_0|^2}{i\omega_b + \kappa_b}. \tag{3b}$$

$|m_0|^2$ and $|b_0|^2$ denote, respectively, the steady-state average magnon number and the phonon number provided by the pumping field Ω_0. According to Equations (3a) and (3b), we can obtain the following function relationship of $|m_0|^2$:

$$\frac{4g_{mb}^4\omega_b^2}{(\omega_b^2+\kappa_b^2)^2}(|m_0|^2)^3 + \frac{4\Delta_m g_{mb}^2\omega_b}{\omega_b^2+\kappa_b^2}(|m_0|^2)^2 + (\kappa_m^2+\Delta_m^2)|m_0|^2 = \frac{5\gamma^2 N\mu_0 P_0}{8Sc}. \tag{4}$$

3. Results and Discussion

We display the steady-state magnon number $|m_0|^2$ as a function of the power of the microwave drive field P_0 for different values of the magnomechanical coupling strength g_{mb} in Figure 2. As shown by the red line in Figure 2, without the magnomechanical coupling, i.e., $g_{mb} = 0$, the steady-state magnon number $|m_0|^2$ undergoes linear growth with increase in the power of the microwave drive field P_0. Interestingly, the steady-state magnon number $|m_0|^2$ experiences a bistable behavior of P_0 in a certain parameter region when we consider the magnomechanical coupling, implying that the magnonic response exhibits two different stable states. As shown by the blue line (corresponding to the magnomechanical coupling strength $g_{mb}/2\pi = 9.88$ mHz) in Figure 2, for the case where $P_0 < 143.1$ mW, only one solution exists and the system has no bistability. For the case where 143.1 mW $< P_0 <$ 8.867 W, the cubic Equation (4) for the steady-state magnon number $|m_0|^2$ yields three real roots. The largest and smallest roots are stable, and the middle one is unstable, which is indicated by the dashed line. The system gives rise to bistability in this region [6,50]. The magnonic bistability can be seen from the hysteresis loop. Specifically, the steady-state magnon number $|m_0|^2$ initially lies in the lower stable

branch (corresponding to the smallest root). When the power of the microwave drive field is gradually increased, the steady-state magnon number $|m_0|^2$ scans the lower stable branch. When the steady-state magnon number $|m_0|^2$ arrives at the end of the lower stable branch, i.e., the first critical point, it jumps to the upper stable branch. After jumping to the upper stable branch, the steady-state magnon number $|m_0|^2$ starts decreasing and still follows the upper stable branch when the power of the microwave drive field is decreased. When the steady-state magnon number $|m_0|^2$ reaches to the second critical point, it jumps down to the lower stable branch. Furthermore, when we increase the magnomechanical coupling strength g_{mb} to 1.1×9.88 mHz, the power of the microwave drive field needed to observe the bistability is relatively lower, as shown by the black line in Figure 2. Here, the power of the pumping field is kept below 10 mW throughout this work to avoid bistability in the system. Specifically, the low-lying excitations indicate $\langle \hat{m}^\dagger \hat{m} \rangle \ll 2Ns$, where $s = 5/2$ is the spin number of the ground state Fe^{3+} ion in the YIG sphere. For a 250-μm-diameter YIG sphere, the total number of spins $N \approx 3.5 \times 10^{16}$ [20]. The magnon number for $P_0 = 10$ mW is about 1.1×10^{14}, which satisfies the assumption of the low-lying excitations $|m|^2 \ll 5N = 17.5 \times 10^{16}$.

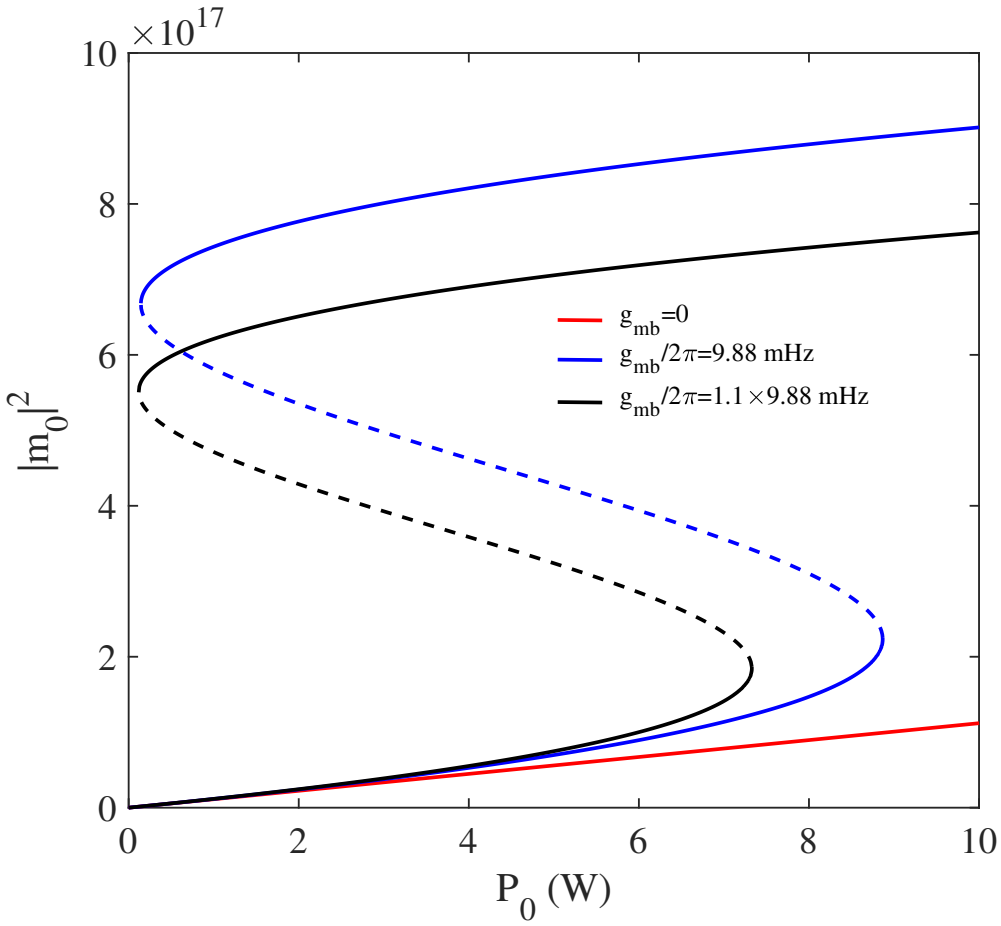

Figure 2. (Color online) Magnon bistability as seen through the steady-state magnon number $|m_0|^2$ varied with the power of the microwave drive field P_0 for the three different magnomechanical coupling strengths $g_{mb}/2\pi = 0$, 9.88 mHz, and 1.1×9.88 mHz, corresponding to the red, blue, and black lines, respectively. The other system parameters we use are $\omega_b/2\pi = 11.42$ MHz, $\kappa_m/2\pi = 0.56$ MHz, $\kappa_b/2\pi = 150$ Hz, and $\Delta_m = \omega_b$, respectively, which are chosen from the recent experiment [20].

By substituting the ansatzs $m = m_0 + \delta m$ and $b = b_0 + \delta b$ into the Equations (2a) and (2b), we can obtain the evolution equation of the perturbations δm and δb made by the probe field:

$$\text{✠}\phi = \mathcal{M}\phi + \mathcal{N}\phi^* + \Omega_p e^{-i\delta t}\sigma, \tag{5}$$

where $\phi = (\delta m, \delta b)^T$, $\sigma = (1, 0)^T$, and

$$\text{✠} = \begin{pmatrix} i\Delta_m + \kappa_m + d/dt & 0 \\ 0 & i\omega_b + \kappa_b + d/dt \end{pmatrix},$$

$$\mathcal{M} = \begin{pmatrix} -ig_{mb}(b_0 + b_0^* + \delta b + \delta b^*) & -ig_{mb}m_0 \\ -ig_{mb}(m_0^* + \delta m^*) & 0 \end{pmatrix},$$

$$\mathcal{N} = \begin{pmatrix} 0 & -ig_{mb}m_0 \\ -ig_{mb}m_0 & 0 \end{pmatrix}.$$

In the perturbative regime, we assume that the perturbations δm and δb can be expressed in the following series form [50]:

$$\delta m = m_1^+ e^{i\delta t} + m_1^- e^{-i\delta t} + m_2^+ e^{2i\delta t} + m_2^- e^{-2i\delta t}, \tag{6a}$$
$$\delta b = b_1^+ e^{i\delta t} + b_1^- e^{-i\delta t} + b_2^+ e^{2i\delta t} + b_2^- e^{-2i\delta t}, \tag{6b}$$

where the coefficients $m_1^\pm$ and $m_2^\pm$ are the amplitude of the magnonic first- and second-order sideband components with the frequency $\omega_0 \mp \delta$ and $\omega_0 \mp 2\delta$, respectively. m_1^+ (m_2^+) and m_1^- (m_2^-) correspond to the lower and upper sidebands, respectively. The physical picture of such ansatzes Equations (6a) and (6b) can be understood as follows: When the Kittel mode in the YIG sphere is excited by the pumping field and the probe field, there are sidebands generated with a series of frequencies $\omega_0 \pm n\delta$, where the integer n is the order of the sideband. These frequency components are generated by the parametric frequency conversion stemmed from the nonlinear terms $-ig_{mb}\delta m(\delta b + \delta b^*)$ and $-ig_{mb}\delta m^*\delta m$, which is quite similar to second- and high-order harmonics generation in a nonlinear medium [51,52]. The first-order upper sideband $\omega_0 + \delta$ is referred to as the anti-Stokes field, and the first-order lower sideband $\omega_0 - \delta$ is known as the Stokes field. The output field with a frequency $\omega_0 + 2\delta$ is the second-order upper sideband, and the frequency $\omega_0 - 2\delta$ is the second-order lower sideband. The third-order sideband and the other higher-order sideband components are very weak in contrast to the second-order sideband and are validly ignored in the perturbative regime. By substituting the ansatzes Equations (6a) and (6b) into the Equation (5), we can obtain

$$m_1^- = \frac{\Omega_p}{\Xi(\delta) - ig_{mb}\lambda m_0}, \tag{7a}$$
$$m_2^- = \frac{ig_{mb}m_0(\Theta + \Upsilon)}{\varpi(\psi_-, \theta) - \rho(\delta)} \tag{7b}$$

where $\Xi(\delta) = i\Delta_m + \kappa_m - i\delta - ig_{mb}(b_0^* + b_0)$, $\lambda = -ig_{mb}m_0^*[1/(-i\omega_b - i\delta + \kappa_b) - 1/(i\omega_b - i\delta + \kappa_b)]$, $m_1^+ = ig_{mb}m_0\lambda^*(m_1^-)^*/\Xi(-\delta)$, $\varpi(x, y) = x - ig_{mb}(b_0 + b_0^*) - ig_{mb}m_0 y$, $\theta = \pi_- m_0^* + (\pi_+ m_0)^*$, $\pi_\pm = ig/(i\omega_b + \kappa_b \pm 2i\delta)$, $\psi_\pm = i\Delta_m + \kappa_b \pm 2i\delta$, $\tau_1 = (\pi_-^* + \pi_+)m_0^*$, $\tau_2 = (\pi_- + \pi_+)m_0$, $\Upsilon = (\pi_- + \pi_+^*)(m_1^+)^* m_1^- + ig_{mb}\lambda(m_1^-)^2$, and

$$\rho(\delta) = \frac{-g_{mb}^2|m_0|^2\tau_2(\pi_-^* m_0 + \pi_+ m_0)}{\varpi(\psi_+, \tau_1)},$$

$$\Theta = \frac{i\tau_2 g_{mb} m_0^* \Upsilon - i g_{mb} \lambda (m_1^+)^* m_1^-}{\omega^*(\psi_+, \tau_1)}.$$

Using the input–output relation [48] $s_{out} = (\Omega_0 + \Omega_p e^{-i\delta t})/\sqrt{\kappa_m} - \sqrt{\kappa_m} m$, we can obtain the output fields of the magnons:

$$\begin{aligned} s_{out} =& \Omega_0/\sqrt{\kappa_m} - \sqrt{\kappa_m} m_0 + (\Omega_p/\sqrt{\kappa_m} - \sqrt{\kappa_m} m_1^-) e^{-i\delta t} \\ & - \sqrt{\kappa_m} m_1^+ e^{i\delta t} - \sqrt{\kappa_m} m_2^- e^{-2i\delta t} - \sqrt{\kappa_m} m_2^+ e^{2i\delta t}, \end{aligned} \tag{8}$$

where the coefficients $\Omega_0/\sqrt{\kappa_m} - \sqrt{\kappa_m} m_0$, $\Omega_p/\sqrt{\kappa_m} - \sqrt{\kappa_m} m_1^-$, and $-\sqrt{\kappa_m} m_1^+$ denote the amplitude of the output fields at the frequencies ω_0, ω_p, and $2\omega_0 - \omega_p$, respectively, and the amplitude of the output fields at the second-order lower sideband with the frequency $3\omega_0 - 2\omega_p$ and the second-order upper sideband with the frequency $2\omega_p - \omega_0$ can be obtained as $-\sqrt{\kappa_m} m_2^+$ and $-\sqrt{\kappa_m} m_2^-$, respectively. Here, we focus on the generation of the second-order upper sideband. To reveal substantially the second-order upper sideband generation process, we define the transmission of the probe field as $t_p = \sqrt{\kappa_m}(\Omega_p/\sqrt{\kappa_m} - \sqrt{\kappa_m} m_1^-)/\Omega_p = 1 - \kappa_m m_1^-/\Omega_p$, and the dimensionless quantity $\eta = |-\kappa_m m_2^-/\Omega_p|$ as the efficiency of the second-order upper sideband generation. Specifically, we scale the output intensity of the second-order upper sideband generation with respect to the intensity of the probe field.

In order to better understand the physical process of the second-order sideband induced by the magnomechanical nonlinearity, in Figure 3a, we plot the transmission ratio of the probe field $|t_p|^2$ as a function of the detuning δ and the power of the pumping field P_0. As shown in Figure 3b, a transmission peak appears at $\delta/\omega_b = 1$, and we find that the transmission characteristics of the probe field exhibit a strong dependence on the pumping field. In detail, when we increase the power of the pumping field to 0.5 mW and 5 mW, the peak values reach about 0.8 and 1, as shown in Figure 3c,d. This implies that the generation efficiency of the first-order upper sideband becomes higher with increase in the power of the pumping field P_0. The first-order upper sideband is derived from the one-phonon upconversion of the pumping field, which is called an anti-Stokes process [46,53,54]. In addition, Figure 3a shows that the transmission peak of the probe field becomes wider and wider with increase in the power of the pumping field. The width of the transmission peak of the probe field is proportional to the steady-state magnon number, i.e., $\Gamma_m = \kappa_m + 4g_{mb}^2 |m_0|^2/\kappa_m$ [45], and the steady-state magnon number $|m_0|^2$ can be enhanced by increasing the power of the pumping field.

Figure 4 shows that the efficiency η of the magnonic second-order sideband generation varies with the detuning δ for different magnomechanical coupling strengths g_{mb}. We can see that the value of η is zero in the case of $g_{mb} = 0$, which means that no magnonic second-order sideband is generated due to the nonlinear terms [i.e., $-ig_{mb}\delta m(\delta b + \delta b^*)$ and $-ig_{mb}\delta m^* \delta m$] are absent. When the magnomechanical interaction is considered, i.e., $g_{mb}/2\pi = 9.88$ mHz, one can find that an obvious magnonic second-order sideband generation can be observed, i.e., $\eta = 1.3 \times 10^{-3}$, which means that the amplitude of the output magnonic second-order sideband is 1.3×10^{-3} of the amplitude of the probe field. The linewidth of the second-order sideband is about 4.2×10^3 Hz, arising from the intrinsic mechanical damping rate and the microwave drive field induced damping rate, which can be obtained as $\kappa_m + 4g_{mb}^2 |m_0|^2/\kappa_m$ [45] and is consistent with the first-order sideband spectrum. The increase in the magnomechanical coupling strength g_{mb} enhances the generation efficiency of the magnonic second-order sideband. By experimentation, the improvement in the magnomechanical coupling strength can be realized by scaling down the YIG sphere size [20].

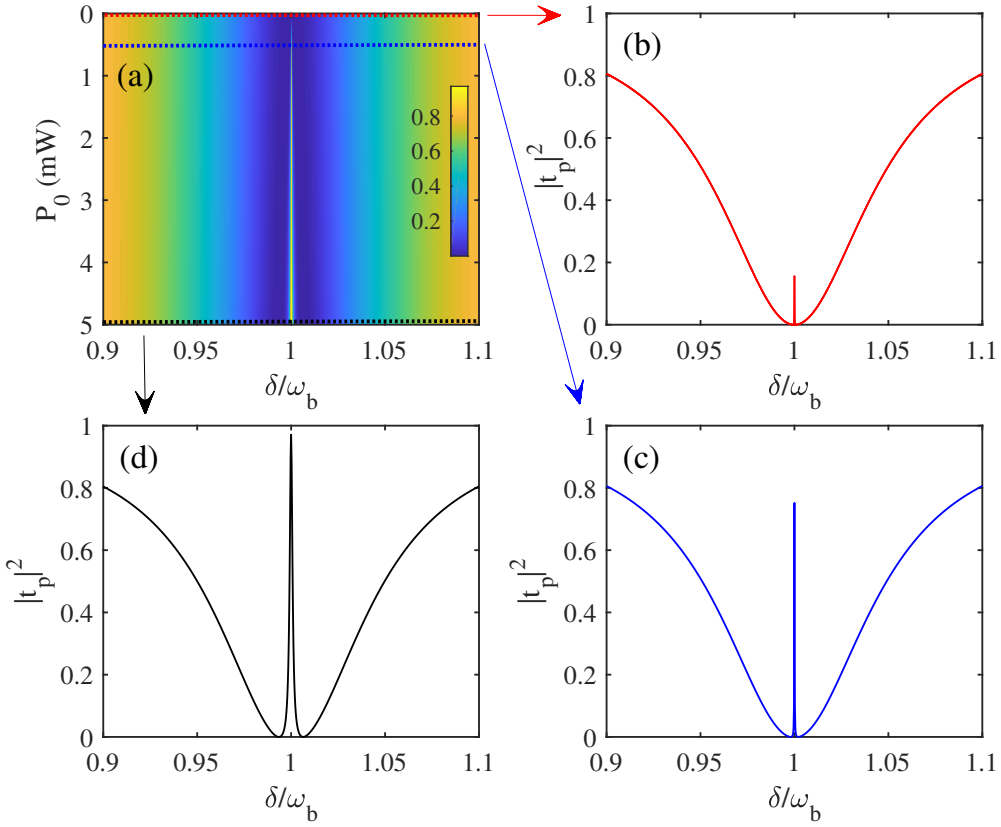

Figure 3. (Color online) (**a**) The transmission spectrum $|t_p|^2$ of the probe field as a function of δ and the power of the pumping field P_0. (**b**–**d**) plot the transmission spectrum $|t_p|^2$ in the case of $P_0 = 10\,\mu$W, 0.5 mW, and 5 mW, respectively. The magnomechanical coupling strength $g_{mb}/2\pi = 9.88$ mHz. We use $\Omega_p/\Omega_0 = 0.05$, and the other parameters are the same as in Figure 2.

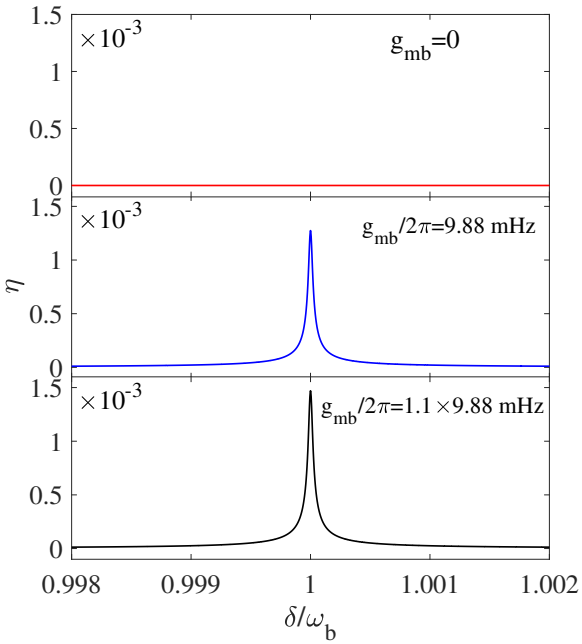

Figure 4. (Color online) The efficiency η of the magnonic second-order sideband generation as a function of the detuning δ for different values of the magnomechanical coupling strength g_{mb}. The power of the pumping field is $P_0 = 10\,\mu$W. The other parameters are the same as in Figure 2.

Figure 5a plots the efficiency η of the magnonic second-order sideband generation varying with the detuning δ and the power of the pumping field. We can see that the

increased pumping field intensity can result in considerable enhancement of the efficiency η. In detail, as shown in Figure 5b–d, the maximum values of the efficiency η are about 4×10^{-3}, 6×10^{-3}, and 6.4×10^{-3}, which correspond to the power of the pumping field $P_0 = 0.1$ mW, 1 mW, 5 mW, respectively. On the other hand, one can find that the efficiency η becomes very small at the resonance point $\delta/\omega_b = 1$. The physical reason for this phenomenon can be understood as follows: The fundamental mechanism for second-order sideband generation is that the anti-Stokes field and the probe field undergo a one-phonon upconverted process. However, destructive interference occurs between the probe field and the anti-Stokes field, which leads to a transparency window at $\delta/\omega_b = 1$, as shown in Figure 3a. Then the generation process of the second-order sideband is subdued at $\delta/\omega_b = 1$ [50]. The linewidth of the second-order sideband becomes wider with increase in the power of the pumping field P_0, while it is much less than the linewith of the magnon resonance mode ($\sim\kappa_m$), such that the magnonic second-order sideband may provide a tool to achieve high-precision measurement.

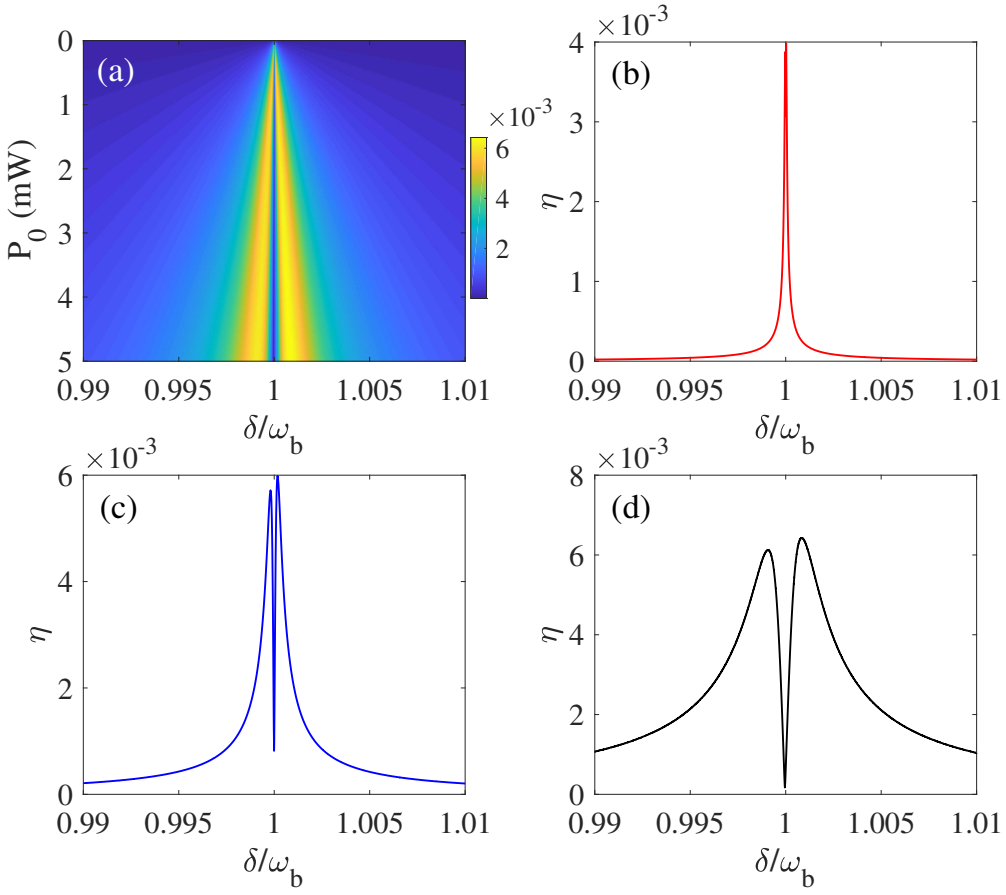

Figure 5. (Color online) (**a**) The contour map of the efficiency η as a function of the detuning δ and the power of the pumping field P_0. (**b**–**d**) plot the spectrum of the magnonic second-order sideband in the case of $P_0 = 0.1$ mW, 1 mW, and 5 mW, respectively. The magnomechanical coupling strength $g_{mb}/2\pi = 9.88$ mHz. The other parameters are the same as Figure 2.

Finally, we discuss the influence of the applied bias magnetic field on the magnonic second-order sideband generation. Figure 6 shows that the efficiency η can be tuned by adjusting the bias magnetic field strength H. For a certain pumping power, we find that the efficiency of second-order sideband generation can be enhanced by tuning the bias magnetic field. The maximum value of the efficiency η is about 15.4×10^{-3} when the bias magnetic field strength $H \approx 280.67$ mT, while the efficiency η is about 6×10^{-3} when $P_0 = 1$ mW, as shown in Figure 5c. This implies that the nonlinear magnetostrictive interaction between the magnon mode and the mechanical mode in the YIG sphere is extremely enhanced. It

can be seen that the sideband efficiency is asymmetric, and the critical value $H = 280.71\,\mathrm{mT}$ corresponds to the frequency of the magnon mode $\omega_m/2\pi = 7.86\,\mathrm{GHz}$. The generation of the magnonic second-order sideband can be well controlled by only tuning the applied bias magnetic field without changing the other system parameters, which provides an effective and feasible way to manipulate the magnetostrictive effect and to realize convenient magnomechanical control.

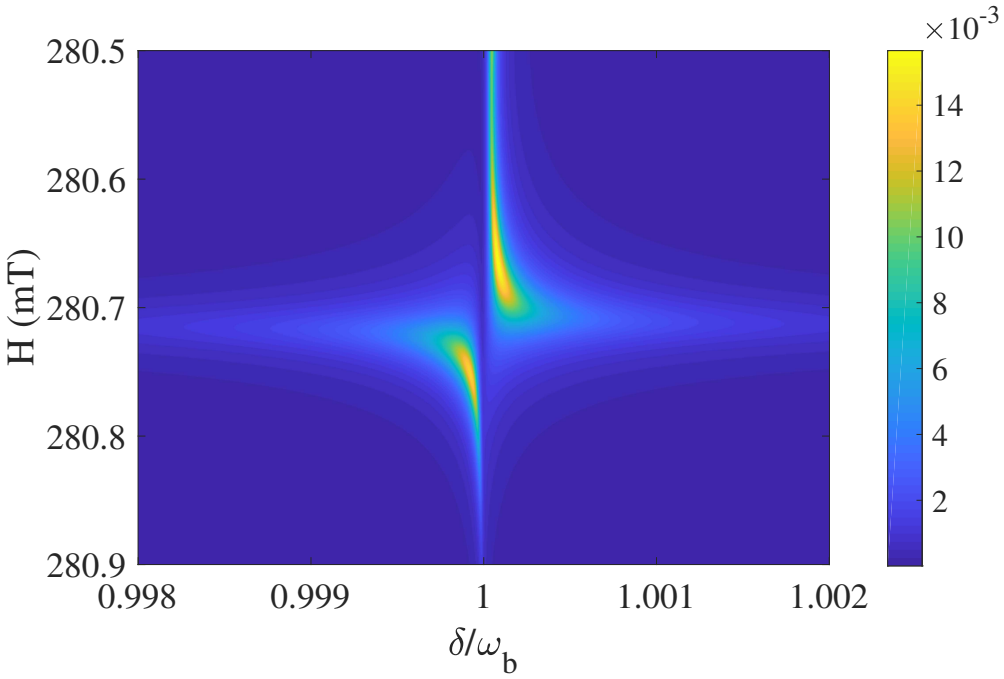

Figure 6. (Color online) The efficiency η as a function of the detuning δ and the bias magnetic field strength H. The power of the pumping field is $P_0 = 1\,\mathrm{mW}$. The other parameters are the same as Figure 5.

4. Conclusions

In conclusion, we have theoretically studied the nonlinear interaction between the magnon mode and the mechanical mode and discussed the generation and control of the magnonic second-order sideband in a magnomechanical system by using the perturbation method. We have shown that the magnomechanical nonlinearity makes the system bistable, and that the magnonic second-order sideband can be tuned by the microwave drive field and the external magnetic field. Based on the low damping and the flexible controllability of the system, the magnonic second-order sideband presented here possesses the features of narrow linewidth and convenient control. Beyond fundamental scientific significance, our results may have potential applications in high-precision measurement, such as force sensors [55], magnetostrictive transducers [56] and actuators [57].

Author Contributions: L.Y. carried out the calculations, wrote the main manuscript text and prepared all the figures; B.W. reviewed the manuscript and contributed to the interpretation of the work and the writing of the manuscript; H.X. participated in the discussions. All authors have read and agreed to the published version of the manuscript.

Funding: This research was funded by the National Natural Science Foundation of China, grant number: 12004202.

Institutional Review Board Statement: Not applicable.

Informed Consent Statement: Not applicable.

Data Availability Statement: Data are contained within the article.

Conflicts of Interest: The authors declare no conflict of interest.

References

1. Chumak, A.V.; Vasyuchka, V.I.; Serga, A.A.; Hillebrands, B. Magnon spintronics. *Nat. Phys.* **2015**, *11*, 453–461. [CrossRef]
2. Soykal, O.O.; Flatte, M.E. Strong field interactions between a nanomagnet and a photonic cavity. *Phys. Rev. Lett.* **2010**, *104*, 077202. [CrossRef]
3. Tabuchi, Y.; Ishino, S.; Ishikawa, T.; Yamazaki, R.; Usami, K.; Nakamura, Y. Hybridizing ferromagnetic magnons and microwave photons in the quantum limit. *Phys. Rev. Lett.* **2014**, *113*, 083603. [CrossRef]
4. Zhang, X.; Zou, C.-L.; Jiang, L.; Tang, H.X. Strongly coupled magnons and cavity microwave photons. *Phys. Rev. Lett.* **2014**, *113*, 156401. [CrossRef] [PubMed]
5. Bai, L.; Harder, M.; Chen, Y.P.; Fan, X.; Xiao, J.Q.; Hu, C.-M. Spin pumping in electrodynamically coupled magnon-photon systems. *Phys. Rev. Lett.* **2015**, *114*, 227201. [CrossRef]
6. Wang, Y.-P.; Zhang, G.-Q.; Zhang, D.; Li, T.-F.; Hu, C.-M.; You, J.Q. Bistability of cavity magnon-polaritons. *Phys. Rev. Lett.* **2018**, *120*, 057202. [CrossRef] [PubMed]
7. Zhang, D.; Wang, X.-M.; Li, T.-F.; Luo, X.-Q.; Wu, W.; Nori, F.; You, J.Q. Cavity quantum electrodynamics with ferromagnetic magnons in a small yttrium-iron-garnet sphere. *NPJ Quantum Inf.* **2015**, *1*, 15014. [CrossRef]
8. Zhang, X.; Zou, C.-L.; Zhu, N.; Marquardt, F.; Jiang, L.; Tang, H.X. Magnon dark modes and gradient memory. *Nat. Commun.* **2015**, *6*, 8914. [CrossRef] [PubMed]
9. Osada, A.; Hisatomi, R.; Noguchi, A.; Tabuchi, Y.; Yamazaki, R.; Usami, K.; Sadgrove, M.; Yalla, R.; Nomura, M.; Nakamura, Y. Cavity Optomagnonics with Spin-Orbit Coupled Photons. *Phys. Rev. Lett.* **2016**, *116*, 223601. [CrossRef] [PubMed]
10. Kusminskiy, S.V.; Tang, H.X.; Marquardt, F. Coupled spin-light dynamics in cavity optomagnonics. *Phys. Rev. A* **2016**, *94*, 033821. [CrossRef]
11. Zhang, X.; Zhu, N.; Zou, C.-L.; Tang, H.X. Optomagnonic Whispering Gallery Microresonators. *Phys. Rev. Lett.* **2016**, *117*, 123605. [CrossRef]
12. Sharma, S.; Rameshti, B.Z.; Blanter, Y.M.; Bauer, G.E.W. Optimal mode matching in cavity optomagnonics. *Phys. Rev. B* **2019**, *99*, 214423. [CrossRef]
13. Xu, Y.-J.; Song, J. Nonreciprocal magnon laser. *Opt. Lett.* **2021**, *46*, 5276–5279. [CrossRef]
14. Liu, Z.-X.; Li, Y.-Q. Optomagnonic frequency combs. *Photon. Res.* **2022**, *10*, 2786–2793. [CrossRef]
15. Fan, Z.; Zuo, X.; Qian, H.; Li, J. Proposal for optomagnonic teleportation and entanglement swapping. *Photonics* **2023**, *10*, 739. [CrossRef]
16. Tabuchi, Y.; Ishino, S.; Noguchi, A.; Ishikawa, T.; Yamazaki, R.; Usami, K.; Nakamura, Y. Coherent coupling between a ferromagnetic magnon and a superconducting qubit. *Science* **2015**, *349*, 405. [CrossRef] [PubMed]
17. Lachance-Quirion, D.; Tabuchi, Y.; Ishino, S.; Noguchi, A.; Ishikawa, T.; Yamazaki, R.; Nakamura, Y. Resolving quanta of collective spin excitations in a millimeter-sized ferromagnet. *Sci. Adv.* **2017**, *3*, e1603150. [CrossRef] [PubMed]
18. Liu, Z.-X.; Xiong, H.; Wu, Y. Magnon blockade in a hybrid ferromagnet-superconductor quantum system. *Phys. Rev. B* **2019**, *100*, 134421. [CrossRef]
19. Spencer, E.G.; LeCraw, R.C. Magnetoacoustic resonance in yttrium iron garnet. *Phys. Rev. Lett.* **1958**, *1*, 241–243. [CrossRef]
20. Zhang, X.; Zou, C.-L.; Jiang, L.; Tang, H.X. Cavity magnomechanics. *Sci. Adv.* **2016**, *2*, 1501286. [CrossRef]
21. Li, J.; Zhu, S.-Y. Entangling two magnon modes via magnetostrictive interaction. *New J. Phys.* **2019**, *21*, 085001. [CrossRef]
22. Xu, G.-T.; Zhang, M.; Wang, Z.-Y.; Wang, Y.; Liu, Y.-X.; Shen, Z.; Guo, G.-C.; Dong, C.-H. Ringing spectroscopy in the magnomechanical system. *Fundam. Res.* **2023**, *3*, 45–49. [CrossRef]
23. Li, J.; Gröblacher, S. Entangling the vibrational modes of two massive ferromagnetic spheres using cavity magnomechanics. *Quantum Sci. Technol.* **2021**, *6*, 024005. [CrossRef]
24. Potts, C.A.; Varga, E.; Bittencourt, V.A.S.V.; Kusminskiy, S.V.; Davis, J.P. Dynamical backaction magnomechanics. *Phys. Rev. X* **2021**, *11*, 031053. [CrossRef]
25. Li, J.; Zhu, S.-Y.; Agarwal, G.S. Magnon-photon-phonon entanglement in cavity magnomechanics. *Phys. Rev. Lett.* **2018**, *121*, 203601. [CrossRef] [PubMed]
26. Yu, M.; Shen, H.; Li, J. Magnetostrictively induced stationary entanglement between two microwave fields. *Phys. Rev. Lett.* **2020**, *124*, 213604. [CrossRef]
27. Fan, Z.-Y.; Qiu, L.; Gröblacher, S.; Li, J. Microwave-optics entanglement via cavity optomagnomechanics. *arXiv* **2022**, arXiv:2208.10703.
28. Shen, R.-C.; Li, J.; Fan, Z.-Y.; Wang, Y.-P.; You, J.Q. Mechanical bistability in Kerr-modified cavity magnomechanics. *Phys. Rev. Lett.* **2022**, *129*, 123601. [CrossRef]
29. Xu, Y.; Liu, J.-Y.; Liu, W.; Xiao, Y.-F. Nonreciprocal phonon laser in a spinning microwave magnomechanical system. *Phys. Rev. A* **2021**, *103*, 053501. [CrossRef]
30. Yang, Z.-B.; Liu, J.-S.; Zhu, A.-D.; Liu, H.-Y.; Yang, R.-C. Nonreciprocal transmission and nonreciprocal entanglement in a spinning microwave magnomechanical system. *Ann. Phys.* **2020**, *532*, 2000196. [CrossRef]
31. Kong, C.; Liu, J.; Xiong, H. Nonreciprocal microwave transmission under the joint mechanism of phase modulation and magnon Kerr nonlinearity effect. *Front. Phys.* **2023**, *18*, 12501. [CrossRef]

32. Wang, X.; Huang, K.-W.; Xiong, H. Nonreciprocal sideband responses in a spinning microwave magnomechanical system. *Opt. Express* **2023**, *31*, 5492–5506. [CrossRef]
33. Li, J.; Wang, Y.-P.; You, J.Q.; Zhu, S.-Y. Squeezing microwaves by magnetostriction. *Natl. Sci. Rev.* **2023**, *10*, nwac247. [CrossRef]
34. Xiong, H. Magnonic frequency combs based on the resonantly enhanced magnetostrictive effect. *Fundam. Res.* **2023**, *3*, 8–14. [CrossRef]
35. Liu, Z.-X.; Peng, J.; Xiong, H. Generation of magnonic frequency combs via a two-tone microwave drive. *Phys. Rev. A* **2023**, *107*, 053708. [CrossRef]
36. Xu, G.-T.; Zhang, M.; Wang, Y.; Shen, Z.; Guo, G.-C.; Dong, C.-H. Magnonic frequency comb in the magnomechanical resonator. *arXiv* **2023**, arXiv:2306.07985.
37. Zhao, J.; Liu, Y.; Wu, L.; Duan, C.-K.; Liu, Y.-X.; Du, J. Observation of anti-PT-symmetry phase transition in the magnon-cavity-magnon coupled system. *Phys. Rev. Appl.* **2020**, *13*, 014053. [CrossRef]
38. Wang, B.; Liu, Z.-X.; Kong, C.; Xiong, H.; Wu, Y. Magnon-induced transparency and amplification in PT-symmetric cavity-magnon system. *Opt. Express* **2018**, *26*, 20248–20257. [CrossRef] [PubMed]
39. Wang, B.; Jia, X.; Lu, X.-H.; Xiong, H. PT-symmetric magnon laser in cavity optomagnonics. *Phys. Rev. A* **2022**, *105*, 053705. [CrossRef]
40. Zhang, G.-Q.; Chen, Z.; Xu, D.; Shammah, N.; Liao, M.; Li, T.-F.; Tong, L.; Zhu, S.-Y.; Nori, F.; You, J.Q. Exceptional point and cross-relaxation effect in a hybrid quantum system. *PRX Quantum* **2021**, *2*, 020307. [CrossRef]
41. Wang, M.; Zhang, D.; Li, X.H.; Wu, Y.Y.; Sun, Z.Y. Magnon chaos in PT-symmetric cavity magnomechanics. *IEEE Photon. J.* **2019**, *11*, 5300108. [CrossRef]
42. Huai, S.-N.; Liu, Y.-L.; Zhang, J.; Yang, L.; Liu Y.-X. Enhanced sideband responses in a PT-symmetric-like cavity magnomechanical system. *Phys. Rev. A* **2019**, *99*, 043803. [CrossRef]
43. Lu, T.-X.; Zhang, H.; Zhang, Q.; Jing, H. Exceptional-point-engineered cavity magnomechanics. *Phys. Rev. A* **2021**, *103*, 063708. [CrossRef]
44. Holstein, T.; Primakoff, H. Field dependence of the intrinsic domain magnetization of a ferromagnet. *Phys. Rev.* **1940**, *58*, 1098. [CrossRef]
45. Aspelmeyer, M.; Kippenberg, T.J.; Marquardt, F. Cavity optomechanics. *Rev. Mod. Phys.* **2014**, *86*, 1391. [CrossRef]
46. Xiong, H.; Wu, Y. Fundamentals and applications of optomechanically induced transparency. *Appl. Phys. Rev.* **2018**, *5*, 031305. [CrossRef]
47. Gardiner, C.W.; Zoller, P. *Quantum Noise*; Springer: Berlin, Germany, 2000.
48. Walls, D.F.; Milburn, G.J. *Quantum Optics*; Springer: Berlin, Germany, 1994.
49. Wang, B.; Lu, X.-H.; Jia, X.; Xiong, H. Coherent stimulated amplification of the skyrmion breathing. *Chaos Solitons Fractals* **2023**, *171*, 113484. [CrossRef]
50. Xiong, H.; Si, L.-G.; Zheng, A.-S.; Yang, X.; Wu, Y. Higher-order sidebands in optomechanically induced transparency. *Phys. Rev. A* **2012**, *86*, 013815. [CrossRef]
51. Ruzicka, B.A.; Werake, L.K.; Xu, G.; Khurgin, J.B.; Sherman, E.Y.; Wu, J.Z.; Zhao, H. Second-harmonic generation induced by electric currents in GaAs. *Phys. Rev. Lett.* **2012**, *108*, 077403. [CrossRef]
52. Velotta, R.; Hay, N.; Mason, M.B.; Castillejo, M.; Marangos, J.P. High-order harmonic generation in laser-aligned molecules. *Phys. Rev. A* **2002**, *65*, 053805.
53. Chen, H.-J. Multiple-Fano-resonance-induced fast and slow light in the hybrid nanomechanical-resonator system. *Phys. Rev. A* **2021**, *104*, 013708. [CrossRef]
54. Chen, H.-J. The fast–slow light transitions induced by Fano resonance in multiple nanomechanical resonators. *Opt. Laser Technol.* **2023**, *161*, 109242. [CrossRef]
55. Yang, Q.; Yan, R.; Fan, C.; Chen, H.; Liu, F.; Liu, S. A magneto-mechanical strongly coupled model for giant magnetostrictive force sensor. *IEEE Trans. Magn.* **2007**, *43*, 1437–1440. [CrossRef]
56. Kim, Y.Y.; Kwon, Y.E. Review of magnetostrictive patch transducers and applications in ultrasonic nondestructive testing of waveguides. *Ultrasonics* **2015**, *62*, 3–19. [CrossRef] [PubMed]
57. Chen, L.; Zhu, Y.; Ling, J.; Feng, Z. Theoretical modeling and experimental evaluation of a magnetostrictive actuator with radial-nested stacked configuration. *Nonlinear Dyn.* **2022**, *109*, 1277–1293. [CrossRef]